Nanoscale

PAPER

Cite this: *Nanoscale*, 2017, **9**, 684

3D multi-energy deconvolution electron microscopy†

Michiel de Goede,‡[a] Eric Johlin,[a] Beniamino Sciacca,[a] Faysal Boughorbel[b] and Erik C. Garnett*[a]

Received 11th October 2016,
Accepted 29th November 2016

DOI: 10.1039/c6nr07991a

www.rsc.org/nanoscale

Three-dimensional (3D) characterization of nanomaterials is traditionally performed by either cross-sectional milling with a focused ion beam (FIB), or transmission electron microscope tomography. While these techniques can produce high quality reconstructions, they are destructive, or require thin samples, often suspended on support membranes. Here, we demonstrate a complementary technique allowing non-destructive investigation of the 3D structure of samples on bulk substrates. This is performed by imaging backscattered electron (BSE) emission at multiple primary beam energies – as the penetration depth of primary electrons is proportional to the beam energy, depth information can be obtained through variations in the beam acceleration. The detected signal however consists of a mixture of the penetrated layers, meaning the structure's three-dimensional geometry can only be retrieved after deconvolving the BSE emission profile from the observed BSE images. This work demonstrates this novel approach by applying a blind source separation deconvolution algorithm to multi-energy acquired BSE images. The deconvolution can thereby allow a 3D reconstruction to be produced from the acquired images of an arbitrary sample, showing qualitative agreement with the true depth structure, as verified through FIB cross-sectional imaging.

1 Introduction

Determining the three-dimensional (3D) structure of a nanomaterial is among the most important types of characterization in nanoscience, due to the strong influence of geometry on a material's optical, mechanical, thermal, electrical, and magnetic properties. In many devices such as transistors, thermoelectrics,[1] batteries,[2] and photovoltaics,[3,4] there are several layers of different materials in which the internal structure and buried interfaces are critical to device operation.

The most commonly used techniques for examining the nanomaterial structure, such as scanning electron microscopy (SEM)[5] and atomic force microscopy (AFM),[6] typically only yield information on the surface topography, neglecting subsurface structural or compositional information. Transmission electron microscopy (TEM) has been used to retrieve the 3D structure of nanomaterials,[7–9] but this method requires thin samples (of the order of 100 nm), often exfoliated onto a support membrane or grid, as well as collection at a wide range of tilt angles (often ~100 images, at angles of ±70° from normal). Alternatively, a focused ion beam (FIB) can be used to mill away parts of a sample, which in conjunction with tilted SEM imaging (FIB-SEM) can provide a cross-sectional view of the internal structure. Repeated slicing and imaging can lead to a full 3D reconstruction,[10,11] although this necessarily destroys the entirety of the sample, and the serial nature of the process makes it difficult to implement over large areas.

While both these techniques can provide excellent spatial resolution down to the nanometer scale,[12,13] a simple and non-destructive technique that can map the 3D structure of large areas of any arbitrary sample (particularly those on bulk substrates of hundreds of microns thickness) would be extremely appealing. Herein we demonstrate a novel technique of multi-energy deconvolution scanning electron microscopy (MEDSEM) allowing for simple, fast and non-destructive mapping of subsurface nanoscale features on arbitrary substrates, using only a SEM; a tool already available in nearly every nanoscience research laboratory.

MEDSEM relies on the energy-dependent electron penetration depth to produce 3D representations of the measured material – increasing the primary beam energy results in deeper electron penetration into the sample,[14] and the backscattering efficiency depends on the atomic number, which allows for elemental contrast.[15] Back-scattered electron (BSE)

[a]*FOM Institute AMOLF, Amsterdam, 1098 XG, The Netherlands*
[b]*FEI Company, Eindhoven, 5651 GG, The Netherlands. E-mail: garnett@amolf.nl; Fax: +31(0)20 754 7290; Tel: +31(0)20 754 7231*

†Electronic supplementary information (ESI) available: Archive .zip file of MATLAB codes for decovolution of image stacks, for 3D rendering of deconvolved images, and documentation. See DOI: 10.1039/C6NR07991A

‡Present address: University of Twente, Enschede, 7522 NB, The Netherlands.

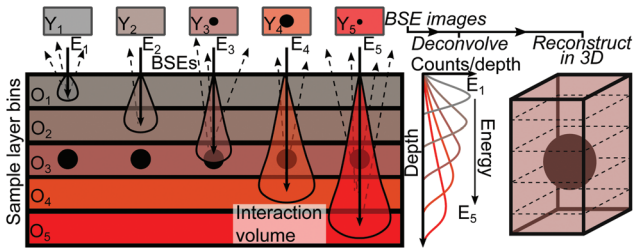

Fig. 1 Schematic of the MEDSEM process. A BSE image is composed of a superposition of virtual depth layers O_i in the measured sample. The mixing extends over deeper layers at higher primary beam energies, which corresponds to the increased depth of the BSE emission volume (left). This is represented by the counts per depth distributions (middle), which shows wider distribution curves at higher energies (increased redness). The deconvolved BSE images are then combined to form a 3D reconstruction of the nanomaterial (right).

emission energy is also depth-dependent, which has been previously investigated for depth-resolved imaging;[16] however, the necessity for *in situ* energy filtering limited such measurements to a few depth slices, and precluded the feasibility of 3D structural rendering. MEDSEM omits this energy filtering, instead retrieving depth information by varying the primary beam energy. While this approach was previously dismissed due to the unavoidable mixing of layer sampling,[16] we show that this can be remedied by applying a blind deconvolution to multiple BSE images obtained at various primary beam energies,[14,17–19] as depicted in Fig. 1.

The deconvolution process treats the nanomaterial structure as consisting of N distinct subsurface layer bins, $O_{n=[1:N]}$. For a set of I images at primary beam energies $E_{i=[1:I]}$, the BSE image Y_i is modeled as a mixing process, assumed to be a linear superposition of these subsurface layer bins. For higher primary beam energies this superposition extends over deeper subsurface layers as the primary electrons produce BSEs from deeper subsurface regions. This translates to

$$Y_i = h_{1,i}O_1 + h_{2,i}O_2 + \ldots + h_{N,i}O_N \quad (1)$$

where $h_{n,i}$ are the energy-dependent mixing weight factors that dictate the mixing between the physical layers that contribute to the observed image (equivalent to the local extent of the point spread function). The task is to simultaneously obtain the best estimates of both $h_{n,i}$ and O_n from the acquired multi-energy BSE images Y_i, preferably without the need for any *a priori* information on the nanomaterial (blind deconvolution). This can be achieved by applying a blind source separation (BSS)[20–22] reconstruction algorithm that solves the acquired multi-energy BSE images for independent images O_n.

2 Results

Our exploration of this new imaging technique proceeds in three sections: first, we demonstrate the MEDSEM procedure by walking through the reconstruction of a 3D rendering of a Ag–Cu_2O core–shell nanowire. Second, we show the ability to volumetrically image features under a solid layer, imaging two Au nanowires underneath a Au sheet, confirming agreement with FIB-SEM cross-sectional measurements. Finally, we apply the method to a multi-layer system, showing the reconstruction of Au–Cu_2O core–shell nanoparticles below two stacked Au–Cu_2O sheets.

2.1 Ag–Cu_2O core–shell nanowire reconstruction

We begin by showing how MEDSEM can be used to retrieve the depth structure of a Ag–Cu_2O core–shell nanowire, synthesized in the method described previously.[23] The nanowire is imaged on a crystalline silicon substrate at 21 primary beam energies in the range E_i = 4–25 keV (see Methods for details).

The influence of the primary beam energy is depicted in Fig. 2a–d – panel a shows the estimated penetration depth of a 4 keV electron beam into a Ag–Cu_2O core–shell nanowire geometry, with the actual BSE image the Ag–Cu_2O core–shell nanowire shown in b. The surface is clearly seen as dominating the electron emission signal, and there is little contrast difference across the wire width. Conversely, at a 12 keV primary beam energy (shown in c and d), we see the electron beam penetrating into the core of the nanowire system in the diagram, and accordingly can now clearly distinguish the brighter core present in the center of the nanowire in the BSE image.

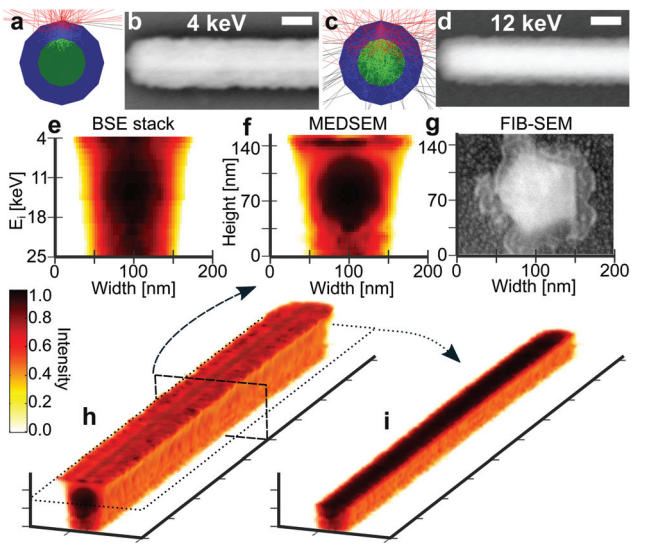

Fig. 2 Ag–Cu_2O core–shell nanowire imaging. a, Diagram of primary electron (gray) and BSE (red) trajectories, and b, BSE SEM image demonstrating surface sensitivity at low acceleration energy, contrasted with c and d, showing high acceleration energy allowing the core of the nanowire to become visible. Scale bars are 100 nm. Cross-sectional slices of BSE image stack, e, before deconvolution, showing smearing between images from acceleration energies E_i, contrasted to the reconstruction, f, after deconvolution, showing the clearly visible core, and the nanowire extent realistically confined. The height is calibrated to the estimated nanowire total thickness. g, Comparison to the FIB-SEM cross-sectional image. h, 3D reconstructions of the core–shell nanowire, with a surface slice through the X–Y plane in i, showing the clearly visible Ag core (black) throughout the imaged length. Tick marks are 200 nm in X and Y, 50 nm in Z. Pixel size is 3.4 nm.

While the simple combination of stacked BSE images at varying energies can thus yield rough depth information, increasing beam energies still contain substantial influences of the preceding layers, as discussed in Fig. 1. In Fig. 2e we show the results of this initial combination of BSE layers as a virtual cross-cut through the nanowire. The convolution of layer information is clearly visible through the smearing of the core region throughout the depth of the wire cross section, as well as a general lack of confinement in the wire structure. As described previously, this influence cannot be removed by image subtraction alone.[16]

Here the benefit of the BSS algorithm becomes clear – after processing with the deconvolution algorithm, the full MEDSEM image in Fig. 2f shows significantly improved clarity of the core–shell nanowire cross section. Specifically, the problems with the raw BSE stack image are largely remedied; the core region is now clearly visible, and the extent of the shell is more reasonably contained. The conversion from energy- to depth-scaling was determined using the dimensions of the nanowire – it was estimated that the lateral and vertical dimensions of the nanowire were roughly similar (an essentially circular cross section), and a linear mapping is applied to the depth slices.

The quality of the deconvolved MEDSEM structure can be further evaluated by comparing it with an actual FIB-SEM cross-cut image in Fig. 2g. Considering the simplicity of this technique, there is reasonable resemblance between the MEDSEM cross-cut and the actual cross-sectional image. The core–shell structure is resolved, and if the nanowire geometry were known, the orientation of the core can also be estimated.

The full 3D reconstruction of the nanowire is shown in Fig. 2h. The quality of the reconstruction is initially not obvious to assess, but by performing a surface slice laterally through the mid-plane of the wire (dashed line), as seen in Fig. 2h, it becomes clear that it is possible to reconstruct the full 3D geometry of the imaged core–shell nanowire using MEDSEM, with the black core region clearly visible throughout the cut-plane image.

2.2 Two-layer nanowire–sheet reconstruction

Next, we demonstrate how MEDSEM can be used to image features through material layers. Here we image a structure composed of two Au nanowires partially lying underneath a thin Au sheet, adjacent to two Au nanoparticles, as shown in the standard BSE image in Fig. 3a.

The MEDSEM 3D reconstruction of the system of nanostructures is shown in Fig. 3b, following the procedure described above with BSE images obtained at 26 equally-spaced energies in the range E_i = 2–28 keV. The nanoparticles are assumed to be roughly spherical, and are used for the depth rescaling. The reconstruction again appears to be reasonably accurate – a separation between the layers of the sample is visible, with the Au sheet resting above the center of the nanowires, with a clearly confined thickness. This is more evident after performing a surface slice through the dotted line in b, as shown in Fig. 3c, elucidating the structure beneath the sheet.

Further confirmation of the MEDSEM reconstruction can be made by comparing a FIB-SEM cross section (taken through the dashed line in Fig. 3a) shown in Fig. 3d, to a cross-sectional slice at the same location in the reconstruction in e. Particularly, the relative sizes and shapes of the nanowire cross sections, with the left elliptical nanowire oriented with its longer axis vertically, and the right nanowire horizontally, as visible in the FIB-SEM cross section, are also captured in the MEDSEM reconstruction.

2.3 Multi-layer sheet–nanoparticle reconstruction

In a final exploration of the applications of this technique, we prepared a sample consisting of Au–Cu_2O core–shell nanoparticles lying underneath two stacked Au–Cu_2O sheets, to show how MEDSEM can be employed to retrieve 3D information of complex multi-layered structures, composed of a variety of materials. A standard BSE image is shown in Fig. 4a, displaying a somewhat ambiguously layered stack of two sheets, above the partially visible core–shell nanoparticles.

The sample was imaged with 28 primary beam energies in the range E_i = 3–29 keV, and the MEDSEM procedure was

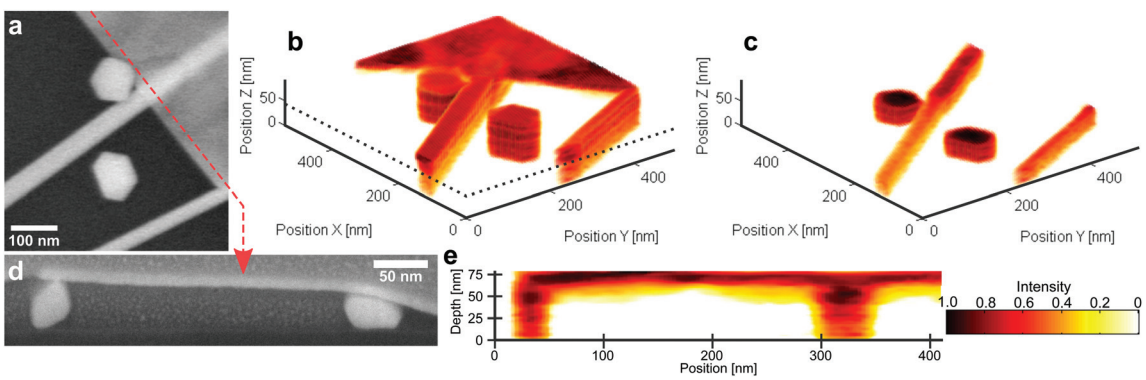

Fig. 3 a, BSE image of an Au sheet on top of two Au nanowires, with two adjacent Au nanoparticles. b, 3D MEDSEM reconstruction of the nanostructure system, as well as a surface slice (dotted line in b) showing the region below the Au sheet in c. Cross-sectional views (taken through the dashed line in a) using FIB-SEM in d, and the MEDSEM reconstruction in e, showing qualitative agreement. Pixel size is 4.5 nm.

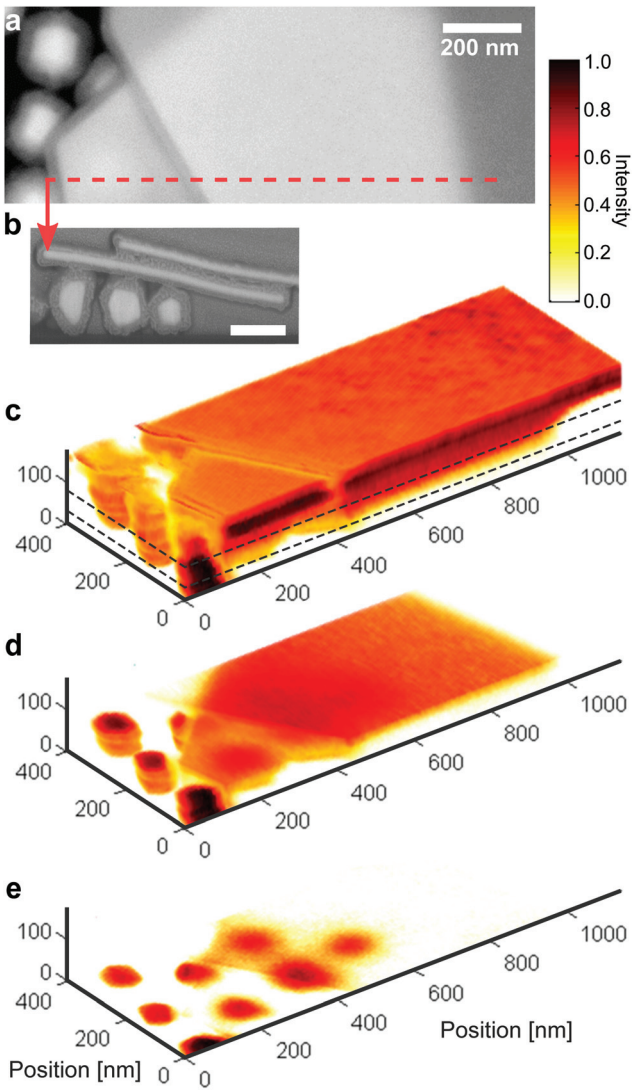

Fig. 4 a, BSE image of a double-layer Au–Cu_2O sheet stack above Au–Cu_2O core–shell nanoparticles. b, FIB-SEM cross section taken at the location indicated by the dashed line in a. c, 3D MEDSEM reconstruction of the nanostructure system. d, e, 3D MEDSEM reconstructions of surface slices through the *X*–*Y* plane (indicated in c), displaying the variations of the imaged system with depth. Pixel size is 2.7 nm.

applied to create a 3D reconstruction, as shown in Fig. 4c, again using the estimated nanoparticle symmetry for depth scaling. This full reconstruction view already clarifies the stacking order of the Au–Cu_2O sheets, and correctly places them over the nanoparticles, both in agreement with the FIB-SEM cross section shown in b. Furthermore, by taking layer slices through the system (as indicated by the dashed lines in c), the geometry of the stacked structures becomes visible: in the first layer slice, shown in Fig. 4d, the structure of the lower (pentagonal) Au–Cu_2O sheet is visible below the larger top sheet. The core–shell geometry of the nanoparticles is also visible from the bisected particle on the left side (x = 100, y = 550) of the reconstruction. The layer geometry is further clarified by a second, lower slice, shown in Fig. 4e. Here we see the ~7.5 core–shell nanoparticles visible in the lowest position in the stack, demonstrating the capability of MEDSEM to reconstruct the depth profile of a complex, multi-stacked system.

3 Discussion

While the results discussed herein establish the ability of MEDSEM to retrieve qualitative information of the subsurface structure of nanomaterial systems, the reconstruction of a 3D structure from BSE images is still not perfect, due to inherent limitations of the model employed. We next discuss two such issues, as well as possible improvements to overcome these limitations.

First, the use of only BSE emission results in surface topography artifacts in the deconvolved images, deviating from the true structure of the measured system. This is expected, as a BSE image is a flat projection of the surface topography and therefore local height differences are not resolvable. This loss of topographic resolution is visible in all three measurements presented here: in the first Ag–Cu_2O nanowire rendering, the FIB revealed a flower-like outer structure of the nanowire, however, the MEDSEM reconstruction projects this topography as a flat surface (Fig. 2i). Similarly, in the Au nanowire/nanosheet measurements, the curvature of the sheet visible in the FIB image is lost in the cross-sectional reconstruction (Fig. 3e). Finally, in the layered system, it is visible in the FIB cross section that the sheets are resting diagonally across the nanoparticles; however in the MEDSEM reconstruction, the system appears completely flat (Fig. 4c and d). Additionally, the position of the exposed nanoparticle (on the far left hand side of Fig. 4d) relative to the other nanoparticles becomes skewed, as the electron beam interacts with different amounts of material between the exposed and covered particles, obfuscating their positions. This results in the exposed particle to appear above those embedded beneath the sheets.

We propose that surface measurements from AFM or possibly tilted SEM imaging could be incorporated into the reconstruction algorithm in order to allow for offsetting of the reconstruction with a displacement from the known surface profile. Alternatively, this loss of topography can be overcome by embedding the nanomaterial in a flat, lower-contrast material. This would cause the electron beam to interact with an amount of embedding material proportional to the surface topography, thereby allowing the original surface structure to be better reconstructed by the deconvolution algorithm.

Second, while MEDSEM provides 3D structural information showing qualitative agreement with the true structure of the imaged system, it does not immediately provide a quantitative measurement of depth dimensions. As shown in Fig. 2, calibration of the deconvolved slices to a quantitative depth can be performed by utilizing known (or estimated) dimensions and using a simple linear mapping of the reconstruction slices to the total depth of a feature. This could be improved through either tilted SEM or AFM measurements providing a calibration of known depths to observable features in the 3D

reconstruction, particularly if the dimensions or rough geometry of the sample are initially unknown.

An alternative method of calibration, avoiding additional measurements or estimates, could be performed through the application of MEDSEM to a wide set of reference samples (experimentally, or using simulations), which would provide a database of the depth–energy relationship. These scalings could then be applied to future measurements on arbitrary structures of known (or estimated) compositions to obtain depth dimensional information, without the need to destroy the measured sample. While an unknown composition could cause distortions from variations in the emission volume, in practice (for the samples measured here), we see qualitative agreement between MEDSEM images and FIB-SEM cross sections, suggesting that this is not a critical issue.

In essence, all aforementioned shortcomings of MEDSEM result from its inherent "blindness," which can be reduced by the inclusion of additional information (some of which could be easily obtainable in the SEM), thereby improving the surface and depth reconstruction capabilities.

4 Conclusions

Herein, we have shown that subsurface features in nanomaterials can be accurately retrieved from BSE images acquired using a range of primary beam energies and applying a BSS deconvolution algorithm based on a simplified image formation model. Despite the employed algorithm requiring no prior information of the sample composition or structure, the results agree qualitatively well with depth profiles obtained from FIB-SEM cross-sectional imaging.

While the reconstructed depth profile is not yet perfect, the visualization of deconvolved 3D structures already allows for analysis that may otherwise not be possible to perform. For example, ensuring the full coating of a core–shell nanowire on a substrate (Fig. 2) would be quite difficult without damaging the sample (through FIB cross-cuts, or thinning of the substrate for TEM), particularly if the interface between the nanowire and the substrate was of interest (*e.g.* to prevent shorting). The convolution between layers prevents imaging of this coating from raw BSE images alone, but after the MEDSEM deconvolution and reconstruction, the full coating is unambiguous.

Furthermore, improvement of the BSS deconvolution can be readily achieved by introducing additional information on the composition or the surface profile. The already promising results, combined with clear routes for future improvements make MEDSEM an attractive new imaging method for electron microscopy, providing easily obtainable 3D information in a fast, non-destructive, and sample-agnostic manner. Finally, the MATLAB codes for the deconvolution and processing, along with a more detailed description of the algorithm, are included in the ESI† to facilitate further use and development of this technique.

5 Methods

Samples were produced by drop-casting nanostructures (produced as reported previously[23,24]) onto clean silicon substrates. Fiducial markings were scribed into the substrates to allow location of the same structures between MEDSEM and FIB-SEM measurements.

BSE image stacks were obtained with a Verios XHR SEM from FEI with a Mirror Detector (MD) and a concentric backscatter detector (CBSD); these were chosen due to their excellent elemental contrast, although other BSE detectors could also be used. The images were obtained at ultra-high magnifications at roughly nanometer sized spatial resolutions for various primary beam energies in the energy range of E_i = 2–29 keV. After the registration and contrast-normalization of the acquired multi-energy BSE images, the BSS deconvolution routine was applied to solve for the deconvolved BSE images O_i.

The image formation model reduces to the matrix equation Y = HO, with Y and O being 3D matrices containing the obtained, and deconvolved BSE images, respectively, and H the 2D mixing matrix. The deconvolution was performed by a multiplicative matrix factorization algorithm that alternately solves for O and H in an iterative manner. In this case, we used the minimization of the alpha-divergence cost function.[25,26] A total variation regularization filtering was applied during the deconvolution, as BSS algorithms are known to inherently introduce noise.[27]

A Helios NanoLab DualBeam from FEI was used to perform FIB-SEM cross-sectional imaging in order to assess the quality of the obtained reconstructions. Samples were coated in a protective platinum layer before FIB cross-sectioning causing the visible material above the interrogated samples in the FIB-SEM images.

Acknowledgements

This work is part of the research program of the Foundation for Fundamental Research on Matter (FOM), which is part of The Netherlands Organization for Scientific Research (NWO). The authors acknowledge financial support from the European Research Council under the European Union's Seventh Framework Programme (FP/2007-2013)/ERC Grant Agreement No. 337328, "NanoEnabledPV", and by a TKI instrumentation grant together with FEI.

References

1 Y. Gao, A. Marconnet, M. Panzer, S. LeBlanc, S. Dogbe, Y. Ezzahri, A. Shakouri and K. Goodson, *J. Electron. Mater.*, 2010, **39**, 1456–1462.
2 H. Wu and Y. Cui, *Nano Today*, 2012, **7**, 414–429.
3 S. Oener, S. Mann, B. Sciacca, C. Sfiligoj, J. Hoang and E. Garnett, *Appl. Phys. Lett.*, 2015, **106**, 023501.

4 E. Johlin, A. Al-Obeidi, G. Nogay, M. Stuckelberger, T. Buonassisi and J. C. Grossman, *ACS Appl. Mater. Interfaces*, 2016, **8**, 15169–15176.
5 H. Seiler, *J. Appl. Phys.*, 1983, **54**, R1–R18.
6 Y. Sugimoto, P. Pou, M. Abe, P. Jelinek, R. Pérez, S. Morita and O. Custance, *Nature*, 2007, **446**, 64–67.
7 S. Van Aert, K. J. Batenburg, M. D. Rossell, R. Erni and G. Van Tendeloo, *Nature*, 2011, **470**, 374–377.
8 C.-C. Chen, C. Zhu, E. R. White, C.-Y. Chiu, M. Scott, B. Regan, L. D. Marks, Y. Huang and J. Miao, *Nature*, 2013, **496**, 74–77.
9 P. Torruella, R. Arenal, F. de la Peña, Z. Saghi, L. Yedra, A. Eljarrat, L. López-Conesa, M. Estrader, A. López-Ortega, G. Salazar-Alvarez, J. Nogués, C. Ducati, P. A. Midgley, F. Peiró and S. Estradé, *Nano Lett.*, 2016, **16**, 5068–5073.
10 J. R. Wilson, W. Kobsiriphat, R. Mendoza, H.-Y. Chen, J. M. Hiller, D. J. Miller, K. Thornton, P. W. Voorhees, S. B. Adler and S. A. Barnett, *Nat. Mater.*, 2006, **5**, 541–544.
11 C. Villinger, H. Gregorius, C. Kranz, K. Höhn, C. Münzberg, G. von Wichert, B. Mizaikoff, G. Wanner and P. Walther, *Histochem. Cell Biol.*, 2012, **138**, 549–556.
12 M. Weyland and P. A. Midgley, *Mater. Today*, 2004, **7**, 32–40.
13 C. J. Peddie and L. M. Collinson, *Micron*, 2014, **61**, 9–19.
14 F. Boughorbel, C. S. Kooijman, B. H. Lich and E. G. T. Bosch, SEM imaging method, *US Patent* 8232523, 2012.
15 G. E. Lloyd, *Mineral. Mag.*, 1987, **51**, 3–19.
16 H. Niedrig and E. Rau, *Nucl. Instrum. Methods Phys. Res., Sect. B*, 1998, **142**, 523–534.
17 F. Boughorbel, E. G. T. Bosch, C. S. Kooijman, B. H. Lich and A. F. De Jong, Charged particle microscopy imaging method, *US Patent* 8581189, 2013.
18 F. Boughorbel, X. Zhuge, P. Potocek and B. Lich, *Microsc. Microanal.*, 2012, **18**(S2), 560–561.
19 A. Belouchrani, K. Abed-Meraim, J.-F. Cardoso and E. Moulines, *IEEE Trans. Signal Process.*, 1997, **45**, 434–444.
20 D. Nuzillard and A. Bijaoui, *Astron. Astrophys., Suppl. Ser.*, 2000, **147**, 129–138.
21 R. A. Neher, M. Mitkovski, F. Kirchhoff, E. Neher, F. J. Theis and A. Zeug, *Biophys. J.*, 2009, **96**, 3791–3800.
22 A. K. Takahata, E. Z. Nadalin, R. Ferrari, L. T. Duarte, R. Suyama, R. R. Lopes, J. M. Romano and M. Tygel, *IEEE Signal Process. Mag.*, 2012, **29**, 27–35.
23 B. Sciacca, S. A. Mann, F. D. Tichelaar, H. W. Zandbergen, M. A. Van Huis and E. C. Garnett, *Nano Lett.*, 2014, **14**, 5891–5898.
24 C.-H. Kuo and M. H. Huang, *Nano Today*, 2010, **5**, 106–116.
25 A. Cichocki, S. Cruces and S.-I. Amari, *Entropy*, 2011, **13**, 134–170.
26 A. Cichocki and S.-I. Amari, *Entropy*, 2010, **12**, 1532–1568.
27 S. Osher, M. Burger, D. Goldfarb, J. Xu and W. Yin, *Multiscale Model. Simul.*, 2005, **4**, 460–489.